Open Archive Toulouse Archive Ouverte (OATAO)

OATAO is an open access repository that collects the work of Toulouse researchers and makes it freely available over the web where possible.

This is a publisher-deposited version published in: http://oatao.univ-toulouse.fr/
Eprints ID: 3096

To link to this article: DOI:10.1109/TNS.2009.2014759
URL: http://dx.doi.org/10.1109/TNS.2009.2014759

Metadata, citation

ve Ouverte

To cite this version: GOIFFON, Vincent. HOPKINSON, Gordon R. MAGNAN, Pierre. BERNARD, Frédéric. ROLLAND, Guy. SAINT-PÉ, Olivier. Multilevel RTS in proton irradiated CMOS image sensors manufactured in a deep submicron technology. *IEEE Transactions on Nuclear Science*, August 2009, vol. 56, n° 4, pp. 2132-2141.
ISSN 0018-9499

Any correspondence concerning this service should be sent to the repository administrator: staff-oatao@inp-toulouse.fr

Multilevel RTS in Proton Irradiated CMOS Image Sensors Manufactured in a Deep Submicron Technology

V. Goiffon, *Member, IEEE*, G. R. Hopkinson, *Member, IEEE*, P. Magnan, *Member, IEEE*, F. Bernard, G. Rolland, and O. Saint-Pé

***Abstract*—A new automated method able to detect multilevel random telegraph signals (RTS) in pixel arrays and to extract their main characteristics is presented. The proposed method is applied to several proton irradiated pixel arrays manufactured using a $0.18\ \mu$m CMOS process dedicated to imaging. Despite the large proton energy range and the large fluence range used, similar exponential RTS amplitude distributions are observed. A mean maximum amplitude independent of displacement damage dose is extracted from these distributions and the number of RTS defects appears to scale well with total nonionizing energy loss. These conclusions allow the prediction of RTS amplitude distributions. The effect of electric field on RTS amplitude is also studied and no significant relation between applied bias and RTS amplitude is observed.**

***Index Terms*—Active pixel sensors (APS), CMOS image sensors (CIS), dark current, proton irradiation, random telegraph signal (RTS).**

I. Introduction

DISPLACEMENT damage induced random telegraph signal (RTS) in the image sensor dark current has been studied during the last fifteen years [1]–[9]. All these studies revealed that this kind of RTS is caused by metastable bulk generation centers located in the depleted volume of the semiconductor. These defects seem to be universal since they have been observed with the same behavior in image sensors manufactured using several CCD and CMOS technologies [9]. The discrete switching amplitudes are known to be proportional to integration time, and several theories are proposed to explain their unexpected high values. Among these, electric field enhancement is the most cited justification of such an intense generation process. Moreover, time constants and amplitudes are known to be temperature activated [2] and these defects have been observed to anneal at temperature below 500 K [8], even some at room temperature [9].

Most of the detection methods used to study RTS pixels are based on amplitude and/or standard deviation thresholds. The use of such techniques limits the number of detectable RTS pixels, and the number of parameters that can be automatically extracted. Therefore, not many studies exist on a large number of multilevel RTS pixels. We have developed a method based on an edge detection technique to automatically detect multilevel RTS and extract their typical characteristics.

After reviewing the existing RTS detection techniques and presenting our motivations to develop a new algorithm, the proposed method is described. In a third part, the first results of this technique are presented on unirradiated and irradiated arrays. The irradiated imagers have been exposed to proton energies ranging from 7.4 MeV to 184 MeV, in several facilities and at fluences ranging from 5×10^9 to $3 \times 10^{11}\ \mathrm{H^+/cm^2}$. Despite the variety of exposure conditions, an exponential maximum amplitude distribution is observed with a constant maximum mean amplitude. The number of RTS defects appears to scale with total non-ionizing energy loss (NIEL) and a significant number of more than 2-level RTS is observed, even on the unirradiated device. Finally, the same measurements are repeated with several photodiode bias conditions. The applied electric field does not seem to have any effect on RTS amplitude whereas it decreases the mean dark current pedestal on which the RTS is superimposed.

II. Multilevel RTS Detection

A. Multilevel RTS Properties

As illustrated in Fig. 1, multilevel RTS can be described by the following parameters: the number of discrete levels, the amplitude A_{nm} of each transition, the characteristic time constants and the mean dark current pedestal on which the discrete fluctuations are superimposed. In contrast to the other parameters, the time constant definition is not straightforward. The time constant of a given level can be defined as the mean time spent on this dark current level. This simple definition is well suited for two level RTS but is not very efficient for studying multilevel fluctuations. More than 2 level RTS can be due to the superimposition of several 2-level RTS centers or by RTS centers with more than two levels per center [5]. In both cases, a potential barrier separating two states should correspond to each transition. Furthermore, a time constant should correspond to each potential barrier. Therefore, the only way to study properly the physical mechanism time constants at the origin of multilevel RTS is to extract the time constant of each identified transition. In this case, the time constant of the transition from level n to level m is the mean time before a transition from level n to level

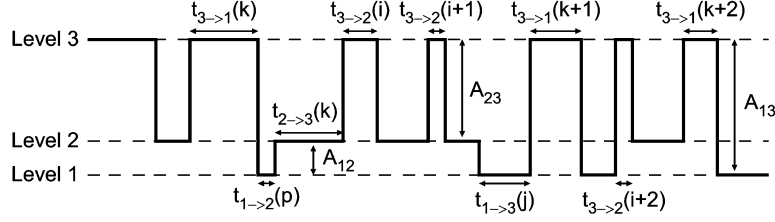

Fig. 1. Three level RTS with its main characteristics. A_{nm} represents the amplitude of transition from level n to level m. The intertransition time i from level n to level m is represented by $t_{n\to m}(i)$.

m occurs: $\tau_{n\to m} = \bar{t}_{n\to m}$. To compute such a transition time constant it is necessary to extract the intertransition time and to associate each extracted intertransition time to the correct transition. This implies that every RTS level and every possible transition has been identified. This reasoning has motivated the search for a detection method able to reconstruct every transition of an RTS.

B. Existing RTS Detection Methods

The following RTS detection methods have been reported: visual counting [2], threshold based methods [4], [7] value histogram analysis [6], statistical properties analysis [10] and the nonscattering pattern method (NSP)[11]. Table I compares these techniques to the method we propose in this paper. The following criteria have been used.

- 2nd col.: Is the method able to detect an RTS?
- 3rd col.: Is the detection process automated or does it need an operator? Can it be used to scan a whole array?
- 4th col.: Is the decision process objective? Is the decision criterion the same for every test condition and every tested device?
- 5th col.: Can the number of discrete levels be extracted?
- 6th col.: Can the level values be extracted?
- 7th col.: Can the level time constants be extracted?
- 8th col.: Can the transition time constants be extracted?

Visual counting and NSP methods main drawbacks are that they can not be automated and that they depend on the operator appreciations. Threshold based methods most often use a criterion based on standard deviation, mean dark current or both to decide which signals are RTS. This is most probably the fastest automated way to count RTS pixels but such methods do not provide RTS characteristics. These techniques can be objective, but have been referred to as nonobjective method in the table since most of the time the threshold is manually tuned for each device and/or each test condition to minimize the false alarm probability. Histogram based methods appear to be a good compromise but their incapacity to extract time constants does not match our needs. Moreover, the decision threshold margin is usually large (five times the standard deviation is cited in [6]) which can be a problem to discriminate the RTS levels. Like the threshold based methods, they are also very sensitive to low frequency drifts which are often observed on long duration RTS measurements. Such drifts change the shape of the value histograms and reduce significantly the detection efficiency. For standard deviation threshold based methods, these drifts can lead to high standard deviations and can then be counted as RTS.

TABLE I
COMPARISON OF RTS DETECTION AND PARAMETER EXTRACTION METHODS. FOR EACH METHOD, THE FOLLOWING FEATURES ARE USED AS CRITERIA FOR THE COMPARISON: RTS DETECTION, AUTOMATED DETECTION, OBJECTIVE DETECTION, NUMBER OF LEVEL EXTRACTION, LEVEL VALUE EXTRACTION, LEVEL TIME CONSTANT EXTRACTION, AND TRANSITION TIME CONSTANT EXTRACTION

Method	Detect.	Auto.	Object.	Level		Time const.	
				No.	Val.	Lvl.	Trans.
Visual	yes	no	no	yes	yes	yes	yes
Threshold	yes	yes	no	no	no	no	no
Histogram	yes	yes	yes	yes	yes	no	no
Statistics	no	-	-	?	yes	yes	?
NSP	yes	no	no	yes	yes	yes	no
Egde det.	yes	yes	yes	yes	yes	yes	yes

Yuzhelevski *et al.* statistical method has been developed to reconstitute 2-level RTS. It supposes that the studied signal has already been identified as RTS and it is not clear if the method can be easily extended to multilevel RTS.

The proposed method is based on the detection of sharp edges in the signal. The detection criterion is universal and does not need to be tuned. If such an edge is detected, the signal is considered as RTS. The dark current values before and after each encountered edge give the levels before and after the transition. The time separating two edges gives the intertransition time. Therefore, all the needed parameters can be extracted. Low frequency drifts can affect the level discrimination but do not affect the RTS detection process. One can note that only one RTS transition is needed to trigger the detection in contrast to most of the cited methods.

C. Proposed Detection Method

1) Method Principle: As presented in Fig. 2, an ideal random telegraph signal can be represented as the succession of rising and/or falling edges in a Gaussian noise background. Like in signal processing applications, the detection of these edges can be done thanks to the convolution of a step shaped filter and the studied signal. The following step shaped filter has been used:

$$H(z) = \frac{2}{L}\left(-\sum_{i=0}^{L/2-1} z^{-i} + \sum_{i=L/2}^{L-1} z^{-i}\right) \tag{1}$$

with L the filter length (the number of coefficients). The number of coefficients is the same before and after the rising edge and it

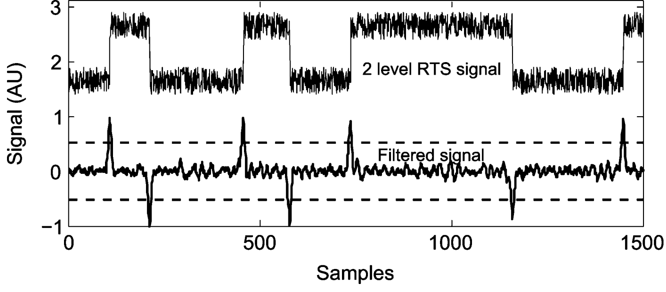

Fig. 2. Method principle illustration. A classical 2-level RTS signal and the same signal after being filtered by the normalized step filter are shown. The dashed lines represent the detection threshold and are equal to the signal standard deviation before filtering. AU stands for arbitrary unit.

is equal to $L/2$. On the high or low state, the coefficient values are equal to each other and the sum of their absolute values is equal to 1. The filter length reduces the Gaussian noise by averaging it whereas the difference between the high and low state values amplifies any encountered edge. The filter output (see Fig. 2) illustrates these properties. The convolution process generates triangles when an edge is encountered. Measuring the peak height of these triangles allows to retrieve the step amplitudes. It is important to notice that the absolute maximum value of the filtered signal represents the largest step amplitude of the signal.

The RTS and the Gaussian noise are supposed uncorrelated, thus the signal variance can be expressed

$$\sigma_{\mathrm{sig}}^2 = \sigma_{\mathrm{RTS}}^2 + \sigma_{\mathrm{gn}}^2 \tag{2}$$

where σ_{RTS} and σ_{gn} are respectively the RTS and the Gaussian noise standard deviations. In order to guaranty a good detection efficiency with a reduced probability of false alarm, the detection condition was set to

$$A_{\max} > \sigma_{\mathrm{sig}} \tag{3}$$

with σ_{sig} the analyzed signal standard deviation and $A_{\max}$ the largest step amplitude, i.e., the maximum absolute value after filtering.

In the worst case, if the time spent on the highest RTS level is close to the time spent on the lowest RTS level, σ_{RTS} can be as high as $A_{\max}/2$. Hence, (2) implies that the following inequality is always verified:

$$\sigma_{\mathrm{sig}}^2 < A_{\max}^2/4 + \sigma_{\mathrm{gn}}^2. \tag{4}$$

Therefore, the detection condition (3) implies that an RTS is detected as long as

$$A_{\max} > \frac{2}{\sqrt{3}}\sigma_{\mathrm{gn}}. \tag{5}$$

The right term of this inequality corresponds to the worst case detection sensitivity. In the best case, the RTS pulse is short enough to have a negligible impact on the signal standard deviation, then $\sigma_{\mathrm{sig}} \approx \sigma_{\mathrm{gn}}$ and the best case detection inequality approaches $A_{\max} > \sigma_{\mathrm{gn}}$. For maximum RTS amplitudes below σ_{gn}, the RTS is not detected.

A false alarm occurs when a non-RTS pixel is detected as RTS. If the signal does not exhibit random switching behavior, $\sigma_{\mathrm{RTS}} = 0$. Then (2) implies that the detection threshold σ_{sig} is equal to σ_{gn}. The Gaussian noise is averaged by the filter on $L/2$ samples. Thus, the Gaussian noise standard deviation after filtering σ_{gnf} is given by

$$\sigma_{\mathrm{gnf}} = \sigma_{\mathrm{gn}}/\sqrt{L/2}. \tag{6}$$

For a signal with no RTS behavior, the absolute maximum filter output value $A_{\max}$ corresponds to the maximum amplitude generated by the Gaussian noise after filtering. According to (3), a false alarm is then generated if the filtered Gaussian noise fluctuations cross the threshold value $\sigma_{\mathrm{sig}} = \sigma_{\mathrm{gn}} = \sqrt{L/2} \times \sigma_{\mathrm{gnf}}$. In other words, the false alarm probability corresponds to the probability that the filtered Gaussian noise fluctuations reach values $\sqrt{L/2}$ times larger than its standard deviation. It can be concluded that the longer the filter, the lower the false alarm probability. However, an RTS transition passes through the filter without attenuation as long as its pulse width is larger than $L/2$. Hence, if the filter is too long, RTS with short time constants will be attenuated like the Gaussian noise. There is so a trade-off to make between false alarm occurrence and the capability to detect the shortest RTS. It is important to notice that, if the filter length is fixed, the sampling rate can be increased to detect the shortest RTS pulses if necessary. In this case the trade-off to make is between the false alarm rate and the amount of data to process, considering a fixed measurement duration.

With these limitations in mind, we chose a filter with 18 coefficients, which means 3^2 points at low or high state. Thus, the Gaussian noise is averaged on 3^2 points and its standard deviation is then reduced by a factor of three after filtering. Since more than 99,7% of the Gaussian distribution values are known to lie within three standard deviations, the theoretical false alarm probability is smaller than 0.3% with this filter length. This result appeared to be a good compromise between filter length and false alarm occurrence. Moreover, the remaining false alarms can be easily suppressed as presented in the next section.

An objective fully automated detection is achieved thanks to the following three step process. First, the signal to analyze is filtered. Then, the filter maximum output value for each signal is stored. Finally, this maximum value is compared to the detection threshold σ_{sig} to decide if the analyzed signal is an RTS or not. This detection process is repeated sequentially on every signal to analyze.

After the detection of an RTS fluctuation and the measurement of its maximum amplitude, it is important to determine the number of discrete levels and to estimate their values. First, the analyzed signal can be sliced up in N_{seg} segments that do not contain any RTS transition. This is easily done from the filtered signal (Fig. 2) by splitting the signal every time a spike is encountered. For each segment i, the mean and the standard deviation are computed and stored in $M_{\mathrm{seg}}(i)$ and $\sigma_{\mathrm{seg}}(i)$ respectively. The Gaussian noise standard deviation is then estimated by averaging the standard deviations $\sigma_{\mathrm{seg}}(i)$. After sorting values contained in the vector M_{seg} by increasing

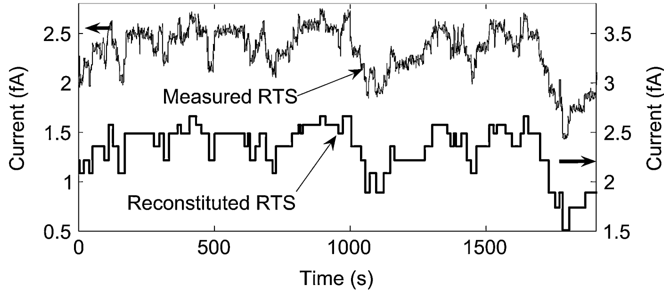

Fig. 3. Result of the proposed algorithm on a proton induced 10 level RTS signal. Both, the analyzed pixel dark current and he signal reconstituted by the detection code are presented. All the levels are recognized and most of the transitions are detected.

order, a new level is finally detected each time a segment mean differs from the detected levels by more than the Gaussian noise standard deviation σ_{gn}.

The RTS signal is reconstituted by associating a level value to each segment. This is done by choosing the closest level to each segment value $M_{\text{seg}}(i)$ and by associating this level to the current segment. At this stage, we can reconstitute a noise free RTS signal by plotting the level values associated with each segment as illustrated in Fig. 3. If two consecutive segments have the same level value, the two segments are concatenated in a longer one. This process increases the detection robustness by simply eliminating any false detection that can occur. Moreover, every transition time index is stored for this reconstitution, then the RTS time constant estimation is straightforward.

As mentioned previously, the detection process is not affected by low frequency drifts. However, the level extraction efficiency can be reduced if a significant low frequency drift appears. In order to improve the robustness of the parameter extraction process, this issue will be addressed in the future by taking into account these drifts in the parameter extraction process.

III. Results and Discussion

A. Experimental Details

The studied CMOS sensor is a custom 128×128 pixel array with classical three transistors (3 T) per pixel design. The area of interest used in this study is constituted by 118×118 pixels. The pixel pitch is 10 μm and the fill factor is about 75%. This circuit was manufactured in a commercial 0.18 μm CMOS technology dedicated to imaging. As described in Table II, eight devices were exposed to proton beams at room temperature. The proton energies range from 7.4 to 184 MeV and the fluences range from 5×10^9 to 3×10^{11} H^+/cm^2. Total NIEL values from [12] have been used for displacement damage dose calculation.

Because of radioactive decay constraints, the devices were stored two months at room temperature before characterization. The effects of room temperature storage on RTS is not precisely known [9], therefore annealing is not taken into account in this paper and it will be studied later more in detail. All the measurements were performed in the dark with temperature regulated to 296.15 K. The tested devices start to saturate for output voltage close to 800 mV. Above this value, the readout chain does not operate in a linear regime. The integration time t_{int} was kept small enough (between 0.1 and 0.8 s) to ensure that the maximum output voltage stay in the linear part of the readout chain. If not specified otherwise, the sensors were operated in soft reset mode (see Section III-F) to reduce the background noise, the measurement duration was about nine hours and the sampling period about 1.6 s. The detection software was not ready before the irradiations. Hence, RTS tests have not been performed on the devices before their irradiation. For comparison, an additional unirradiated device (IC9) was scanned by the RTS detection code.

TABLE II
Irradiation Details. TID and DDD Stand for Total Ionizing Dose (in Gy(Si)) and Displacement Damage Dose Respectively. DC Pre/Post Means Dark Current Measured on Pixel Arrays Before and After Proton Irradiation

IC Nb.	Facility	Energie (MeV)	Fluence (cm^{-2})	TID (Gy)	DDD (TeV/g)	DC pre/post (fA)
1	KVI	50	$8.8\,10^9$	14	34.2	0.14/ 0.58
2	KVI	100	$1.5\,10^{10}$	14	38.9	0.14/ 0.51
3	KVI	184	$2.4\,10^{10}$	14	48.3	0.16/ 0.61
4	KVI	50	$2.0\,10^{10}$	32	77.6	0.14/ 1.07
5	KVI	50	$5.0\,10^9$	8	19.4	0.14/ 0.43
6	Isotron	7.4	$3.2\,10^9$	22	31.6	0.15/ 0.59
7	UCL	62	$1\,10^{11}$	134	340.9	0.18/ 3.94
8	UCL	62	$3\,10^{11}$	402	1022.8	0.25/ 12.1
9	-	-	0	0	0	0.15/ -

In this paper, background noise refers to every temporal noise component except RTS. Therefore, background noise is constituted by readout noise, reset noise and dark current shot noise. The resulting noise is roughly assumed to be a white Gaussian noise in this paper for simplicity purpose. The sum of output referred readout and reset noises is about 280 μV in soft reset mode and 450 μV in hard reset mode. This contribution dominates at the lowest displacement damage doses and the equivalent current noise referred to the photodiode cathode is about 0.02 fA in soft reset mode. For displacement damage doses greater than 100 TeV/g, dark current shot noise dominates. Its mean theoretical value has been evaluated thanks to $\sqrt{qI/t_{\text{int}}}$ and reaches 0.05 fA in IC7 after 341 TeV/g and 0.12 fA in IC8 after 1 GeV/g. It is important to notice that the measurement environment was very stable during the experiment and no significant low frequency drift has been observed on the measured pixel responses.

B. General Observations

Fig. 4 shows the distribution of pixel dark current mean for the following pixel types: regular pixels and RTS pixels with even number of levels. Whatever the number of levels, the mean dark current distribution shapes of RTS pixels are quite the same and look like the well known proton induced dark current distribution: a Gaussian [13] or Gamma [14] distribution around the mean and a tail of bright pixels. The main contribution to the Gaussian shaped part is attributed to elastic interactions whereas the tail has been attributed to both inelastic interactions [15] and electric field enhancement [4]. However, in this technology dedicated to imaging, photodiode doping concentrations are pretty

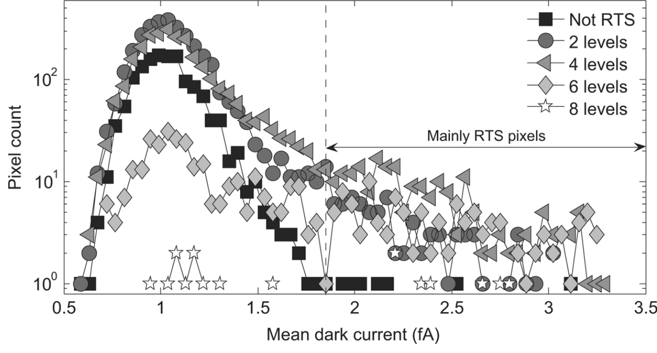

Fig. 4. Mean dark current distributions for regular pixel, 2-level, 4-level, 6-level and 8-level RTS pixels of IC4. RTS pixels with an odd number of levels were not plotted for more clarity.

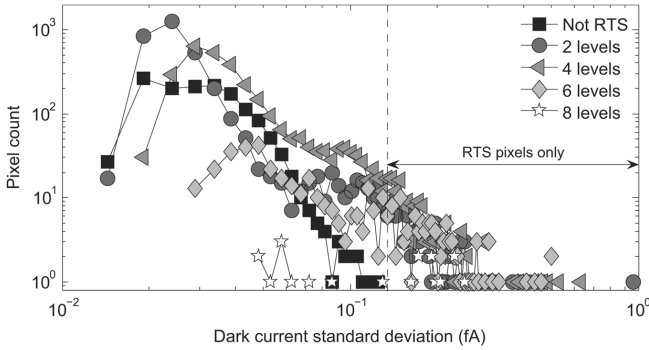

Fig. 5. Dark current standard deviation distributions for regular pixel, 2-level, 4-level, 6-level and 8-level RTS pixels of IC4. RTS pixels with an odd number of levels were not plotted for more clarity.

low in comparison to the ones used in standard CMOS technologies. Furthermore, the photosensitive junction shape has been optimized to reduce electric field peaks. Thus, very high electric fields are not expected and electric field enhancement is not supposed to play a dominant role in this device.

On the other hand, the distribution of pixels without RTS in Fig. 4 does not have a significant bright pixel tail. This suggests that the bright pixel tails usually observed on dark current distributions are mainly constituted by RTS pixels as mentioned in [3]. Nevertheless, the main part of the RTS pixel population is located in the Gaussian area. Hence, a detection method based only on an amplitude threshold will miss most of the RTS pixels. The same conclusion can be made about the dark current standard deviation presented in Fig. 5: a standard deviation above which all the pixels exhibit RTS can be found, but the main part of the RTS pixel population is located in the low standard deviation part of Fig. 5. As it can be expected, the mean standard deviation increases when the number of RTS levels increases.

C. Amplitude Distributions

In order to correctly interpret the amplitude distributions, it is necessary to model the detection probability $P_{\rm dt}$. Let $N_{\rm dt}$ be the number of detected RTS pixels and $N_{\rm rts}$ the number of RTS centers in the whole array. The array is constituted by $N_{\rm pix}$ pixels. The detection probability can be defined as $P_{\rm dt} = N_{\rm dt}/N_{\rm rts}$. A pixel is counted as an RTS pixel if one or more RTS centers with a maximum amplitude greater than the minimum detection sensitivity $D_{\rm sv} \approx \sigma_{\rm gn}$ are located in the pixel. In term of probability it means

$$N_{\rm dt} = N_{\rm pix} \times P(A_{\rm rts} \geq D_{\rm sv}) \times P(n_{\rm rts} \geq 1) \tag{7}$$

where $P(A_{\rm rts} \geq D_{\rm sv})$ is the probability to have an RTS center with a maximum amplitude $A_{\rm rts}$ greater than $D_{\rm sv}$, $P(n_{\rm rts} \geq 1)$ the probability to have one or more RTS defects per pixel and $n_{\rm rts}$ the number of RTS defects per pixel. This number is assumed to be governed by the Poisson law:

$$P(n_{\rm rts} = k) = \frac{\lambda^k e^{-\lambda}}{k!} \tag{8}$$

with $\lambda = N_{\rm rts}/N_{\rm pix}$. Hence, $P(n_{\rm rts} \geq 1) = 1 - e^{-\lambda}$. The detection probability is then given by

$$P_{\rm dt} = \frac{N_{\rm dt}}{N_{\rm rts}} = P(A_{\rm rts} \geq D_{\rm sv}) \times \frac{(1 - e^{-\lambda})}{\lambda}. \tag{9}$$

This probability approaches $P(A_{\rm rts} \geq D_{\rm sv})$ at low fluence when the number of RTS defects is much lower than the number of pixels (i.e., $\lambda \to 0$). It decreases when the number of RTS defects increases and it approaches zero when $\lambda \to \infty$. Therefore, if $P(A_{\rm rts} \geq D_{\rm sv})$ is not close to one the real number of RTS defects $N_{\rm rts}$ can not be estimated correctly.

The situation is different if we consider only the number $N'_{\rm rts}$ of RTS defects with maximum amplitude greater than a chosen value $V_{\rm ch}$. If we choose $V_{\rm ch} > D_{\rm sv}$, the probability to detect the RTS defects with maximum amplitude greater than $V_{\rm ch}$ becomes

$$P'_{\rm dt} = \frac{N'_{\rm dt}}{N'_{\rm rts}} = \frac{(1 - e^{-\lambda'})}{\lambda'} \tag{10}$$

where $\lambda' = N'_{\rm rts}/N_{\rm pix}$. This probability approaches one if the chosen $V_{\rm ch}$ is high enough to ensure $\lambda' \ll 1$. In other words, it is possible to find an amplitude above which the number of detected RTS pixels is close to the number of RTS centers ($N'_{\rm det} \approx N'_{\rm rts}$). One can note that the lower is the displacement damage dose the lower is this amplitude.

The maximum RTS amplitude distributions of representative ICs are presented in Fig. 6. When several RTS amplitudes are observed in a pixel response, the maximum RTS amplitude of a pixel is the largest RTS transition observed for each pixel. The extreme amplitude values are not shown for improved clarity but maximum values range from 1.5 to 8.5 fA in irradiated devices. The number of pixels presenting RTS behavior in the unirradiated device, about 8 %, is quite high compared to previous work but can be partly explained by the use of a more sensitive detection method. About ten percent of these RTS pixels were randomly selected and visually checked. All the checked pixels exhibited clear RTS behavior with the same characteristics as proton induced RTS.

All the distributions exhibit an exponential tail for the highest amplitude values. Since we have just shown that $N'_{\rm det} \approx N'_{\rm rts}$ for the highest RTS amplitudes, the exponential tail is supposed to represent well the real RTS center distribution. This assumption is verified in the next section. These exponential tails have been fitted by the following exponential function:

$$F(x) = \frac{N_{\rm fit}}{\bar{A}_{\rm rts}} e^{-x/\bar{A}_{\rm rts}} \tag{11}$$

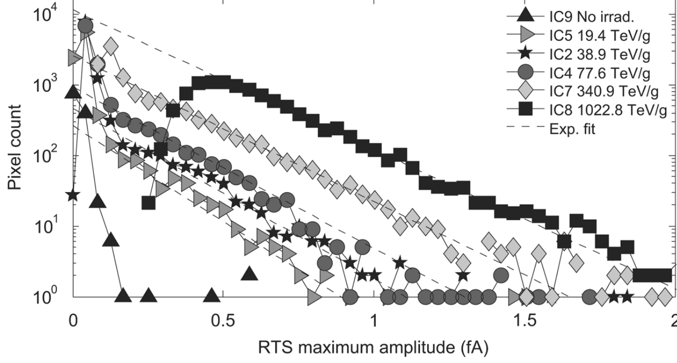

Fig. 6. RTS maximum amplitude distributions. Exponential fits of the distribution tails are also presented.

where $N_{\rm fit}$ is the total number of RTS centers and $\bar{A}_{\rm rts}$ the mean largest RTS amplitude. As it can be seen on the distribution slope, this last parameter does not seem to be a function of fluence or proton energy and the mean achieved value is 0.19 fA with a 0.03 fA standard deviation. It suggests that a universal maximum amplitude exists for radiation induced RTS and that its value is about 0.19 fA per RTS center at 23 °C. This assumption has to be verified on other devices, other test conditions and especially on a larger number of pixels. Nuns *et al.* observed previously exponential amplitude distributions [7]. They found a mean maximum amplitude value of 11.5 pA/cm^2 at -5 °C on a 24 μm-pitch CCD irradiated by 10 MeV protons at a 10^9 H$^+$/cm^2 fluence. Using the 0.44 eV activation energy cited in this paper, we find the following extrapolated value at 23 °C: $\bar{A}_{\rm rts} = 0.4$ fA. This value is in quite good agreement with the value given above if we take into account all the sources of error such as the exponential fit, the small pixel population, the extrapolation to 23 °C, the differences in device types, in detection methods and in storage time/temperature.

In the Shockley-Read-Hall (SRH) theory [16], the worst case dark current that a single level defect can generate is given by [4]

$$I_{\rm defect} = \sigma v_{\rm th} q n_i \tag{12}$$

where σ is the effective capture cross section, $v_{\rm th}$ the thermal velocity, q the elementary charge and n_i the intrinsic carrier concentration. At 23 °C, $I_{\rm defect}$ is only 0.01 fA with a worst case effective cross section of 10^{-15} cm^2 and with the following typical values [17] $v_{\rm th} = 10^7$ cm/s, $n_i = 0.7 \times 10^{10}$ cm^{-3} and $q = 1.6 \times 10^{-19}$ C. As already mentioned in previous work [1], [4], the measured RTS amplitudes are far greater than these worst case values (from 10 to 850 times larger), indicating that another process is involved. This is discussed more in detail in Section III-F.

As regards the low amplitude part of Fig. 6, all the distributions except IC8 plot exhibit a peak shaped distribution. Such a peak distribution has not been reported before. The presented method capability to detect very small RTS fluctuations can explain why. The sharp decrease in the first amplitude bins in Fig. 6 can be interpreted thanks to the detection probability expression (9). First, for low displacement damage doses, the noise background is low and the probability $P(A_{\rm rts} \geq D_{\rm sv})$ that RTS amplitudes are greater than the detection sensitivity $D_{\rm sv}$ is equal to one in all the bins except the first. Hence, the number of counted RTS pixels is underestimated in the first bin leading to the observed drop in Fig. 6. As already discussed, the other term of (9), $(1 - e^{-\lambda})/\lambda$, is significantly lower than unity only for small maximum RTS amplitude values and then contributes to the underestimation of RTS pixel at low maximum amplitude. When the displacement damage dose increases, the probability to have more than one RTS center per pixel increases, and the detection probability drop observed at low amplitude is dominated by the reduction of $(1-e^{-\lambda})/\lambda$. As mentioned previously, the higher is the displacement damage dose, the higher is the amplitude above which $(1 - e^{-\lambda})/\lambda \approx 1$. In other words, the more a device is irradiated, the less small amplitude RTS centers participate to the maximum amplitude value of RTS pixels. IC7 and IC8 curves clearly confirm this assumption since the peak vanishes when the displacement damage dose increases.

The peak value itself could be due to false alarms since it is constituted by small amplitude signals. Like for the unirradiated device, a large number of RTS pixels with amplitudes smaller than or close to the peak values have been visually checked in every device. No obvious false alarm has been observed. Every detected RTS pixel we checked exhibited at least one clear discrete switching. Moreover, this peak rises and shifts slightly toward higher amplitudes when the displacement damage dose increases. This indicates that it is a radiation induced contribution. However, we will not study further this part of the distribution in this paper for the following reasons. First, the detection probability $P_{\rm dt}$ is too low in this region. Hence, the observed distribution does not correspond to the real RTS defect distribution. Second, low amplitude RTS are close to the background noise level and we preferred to focus first on higher amplitudes RTS which are the most important from the user point of view. This peak distribution needs a dedicated study and will be studied in future work.

D. *RTS Defect Counting*

Fig. 7 presents three possibilities to count RTS defects. The most straightforward way is to count the number of detected RTS pixels $N_{\rm dt}$. This number does not vary much with irradiation. This can be explained by the fact that when the number of RTS defects increases, $P_{\rm dt}$ decreases and the resulting number of detected RTS pixels stays almost constant in the displacement damage range used in this paper. This is illustrated by the maximum values of $P_{\rm dt}$ in Table III. The real number of RTS defects $N_{\rm rts}$ is supposed to be greater than both the number of detected RTS pixels $N_{\rm dt}$ and the number estimated from the exponential fit $N_{\rm fit}$. Hence, the maximum value of $P_{\rm dt}$ is achieved by taking $P(A_{\rm rts} \geq D_{\rm sv}) = 1$ and $\lambda = N_{\rm max}/N_{\rm pix}$ with $N_{\rm max} = \max(N_{\rm dt}, N_{\rm fit})$.

The second RTS population indicator is $N_{\rm fit}$, which represents the total number of RTS defects assuming a purely exponential maximum amplitude distribution. In other words, the low amplitude peak is neglected and is supposed to be replaced by an exponential distribution. It leads to an estimated number of defects much larger than the number of pixels for the highest displacement damage dose since the exponential fit is above

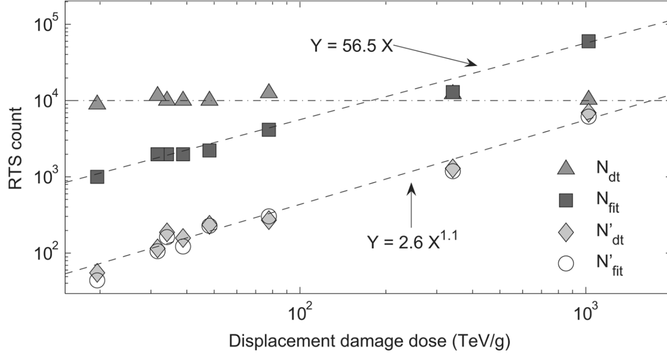

Fig. 7. Evolution of the number of RTS defects with displacement damage dose. $N_{\rm dt}$ is the total number of detected RTS pixels, $N_{\rm fit}$ the total number of RTS defects estimated with the exponential fit, $N'_{\rm dt}$ the number of detected RTS pixels with maximum amplitude greater than 0.5 fA and $N'_{\rm fit}$ the estimated number of RTS defects with maximum amplitude greater than 0.5 fA.

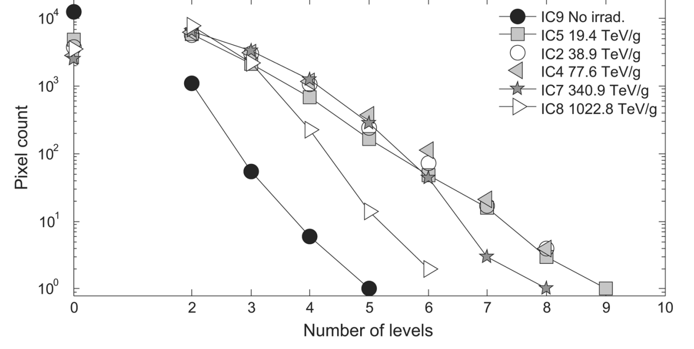

Fig. 8. Distribution of the number of RTS levels in IC9, IC5, IC2, IC4, IC7 and IC8. IC1, IC2, IC3 and IC6 received similar displacement damage doses and have approximately the same RTS level distribution. For improved clarity, only IC2 is shown to represents these last distributions.

TABLE III
RTS COUNT FOR EACH DISPLACEMENT DAMAGE DOSE. THE DETECTION PROBABILITIES ARE ALSO INDICATED. $N'_{\rm dt}$, $N'_{\rm fit}$ AND $P'_{\rm dt}$ ARE DETERMINED FOR MAXIMUM RTS AMPLITUDE GREATER THAN 0.5 FA

DDD	Measure		Estimation (exp.)		$P_{\rm dt}$ max.	$P'_{\rm dt}$
(TeV/g)	$N_{\rm dt}$	$N'_{\rm dt}$	$N_{\rm fit}$	$N'_{\rm fit}$	(%)	(%)
19	8990	56	1000	44	< 74	100
32	11373	115	2000	106	< 68	99
34	9937	190	2000	164	< 71	99
39	10135	158	2000	124	< 71	99
48	10079	238	2200	227	< 71	100
78	12501	334	4200	302	< 66	99
341	12100	1278	13000	1202	< 65	96
1023	10317	6867	60000	6182	< 23	84

the measured IC8 distribution for the lowest maximum amplitudes in Fig. 6. At low displacement damage doses, $N_{\rm fit}$ is lower than the number of detected RTS pixels since the exponential fit does not take into account the peak shaped part of the distribution for low maximum amplitude values. Nevertheless, $N_{\rm fit}$ is a good indicator of the most interesting part of the RTS population. One can notice on the figure that $N_{\rm fit}$ increases linearly with displacement damage dose whatever the proton energy. The same comparison—not presented in this article—was done with the number of elastic events then with the number of inelastic events. A very poor fit was achieved in both cases for the extreme proton energy values (7.4 MeV and 200 MeV). This suggests that elastic and inelastic interactions both contributes to the RTS center creation process and that this process scales with total NIEL as it was concluded in [9] and [5]. The estimated number of RTS defects $N_{\rm fit}$ generated per displacement damage energy deposited appears to be about 56.5 RTS centers per (TeV/g) in this pixel array. This corresponds to about 47 centers $\cdot$ cm^{-3} $\cdot$ (MeV/g)$^{-1}$. With the use of the mean maximum amplitude extracted in the previous section, the most interesting part of RTS amplitude distributions can then be predicted using (11).

The same conclusion can be inferred from the number $N'_{\rm dt}$ of detected RTS pixels with amplitudes greater than $V_{\rm ch} = 0.5$ fA. This number also rises almost linearly ($\propto x^{1.1}$) with displacement damage dose. We chose to count the amplitudes above 0.5 fA because all the distributions are exponential beyond this amplitude. Thus, it can be inferred that for amplitudes greater than 0.5 fA, the number of detected RTS pixels is close to the number of RTS defects. This is confirmed by the high detection probability $P'_{\rm dt}$ presented in Table III. This probability has been computed thanks to (10) with $N'_{\rm rts}$ replaced by $N'_{\rm fit}$.

E. Number of Levels

The distribution of the number of detected levels per pixel is presented in Fig. 8. Multilevel RTS can be caused by either a sum of two or more 2-level RTS centers, one or more multilevel RTS centers or the combination of both [5]. If the sum of independent 2-level RTS center hypothesis is considered, the observed number of levels should be equal to powers of two [1]. It will then be assumed that a number of levels $N_{\rm lvl}$ that does not correspond to a power of two is in fact equal to the closest power of two greater than $N_{\rm lvl}$. The missing levels are assumed to be missed during the level counting process. Therefore, the number of pixels with n defects per pixel $N_{\rm pix}(N_{\rm def} = n)$ is retrieved from the number of pixels with k levels per pixel $N_{\rm pix}(N_{\rm lvl} = k)$ as given by

$$N_{\rm pix}(N_{\rm def} = n) = \sum_{k=1+2^{(n-1)}}^{2^n} N_{\rm pix}(N_{\rm lvl} = k). \quad (13)$$

The resulting distribution for the unirradiated device is compared to a Poisson distribution with $\lambda = 0.1$ in Fig. 9. The Poisson distribution has been multiplied by the total number of pixels to be compared with the measurements. Both distributions match quite well. The number of detected defects is slightly below the expected number, but this can be easily explained by the nonperfect level detection process and the approximations done by using the previous equation. This clearly shows that the independent 2-level RTS center theory can explain the multilevel RTS observed on the unirradiated device.

We tried to use the same approach on irradiated devices. However the probability to have 2-level RTS pixels in comparison to more than 2-level RTS pixels is very high and can not be explained by a Poisson law. The fluences are supposed too high to correctly detect all the RTS levels. The radiation induced noise

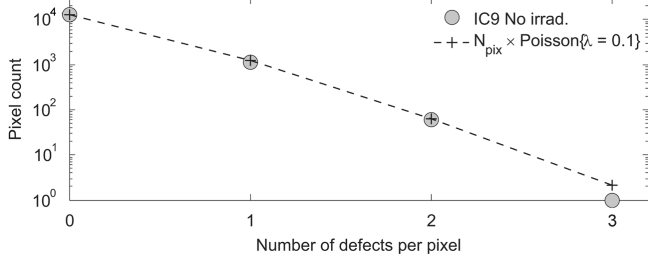

Fig. 9. Distribution of the number of defects per pixel compared to the Poisson distribution with $\lambda = 0.1$. The number of defects per pixel is estimated from the number of level distribution thanks to (13).

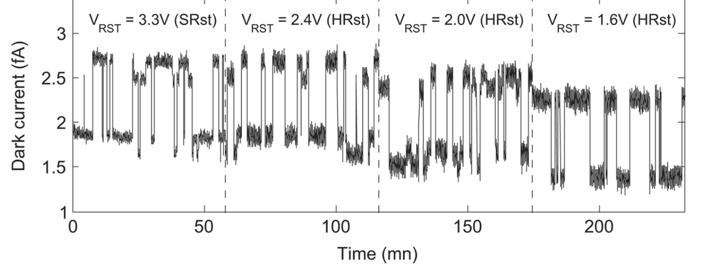

Fig. 10. 4-level RTS measured at 4 different reset conditions. This response was extracted from an IC4 pixel. SRst stands for soft reset and Hrst for hard reset.

is supposed to reduce the level detection efficiency and change the distribution shape. This is confirmed by the decrease of the number of pixels with more than two levels observed in Fig. 8 when the displacement damage dose increases. This suggests that the number of multilevel RTS, in comparison to 2-level RTS, should be greater than what is observed. At the fluences used in this paper, it is likely that a large part of the observed multilevels are the contribution of two or more RTS centers. Moreover, previous work [9] has shown that some multilevel RTS, such as multistable ones, can not be explained by independent centers. Therefore, RTS level numbers seem underestimated and should be studied on devices exposed to lower fluences than what we used but on larger pixel arrays to ensure good statistics.

F. Photodiode Bias Effect

In order to see the influence of applied electric field on RTS behavior, dark current fluctuations were measured during one hour at several photodiode reverse biases. During reset, photodiode cathode voltage can be adjusted by changing the reset voltage V_{RST}. This is only true in hard reset mode. This operating mode [18] corresponds to $V_G - V_{\mathrm{RST}} > V_{\mathrm{th}}$ with V_G and V_{th} the reset transistor gate voltage and threshold voltage respectively. On the contrary, in soft reset mode when $V_{\mathrm{RST}} > V_G - V_{\mathrm{th}}$, the photodiode cathode voltage is pinned to $V_G - V_{\mathrm{th}}$ at the end of the reset phase. In this device, the transition between hard and soft reset was found to be close to 2.4 V. Therefore, for V_{RST} greater than 2.4 V the photodiode is reset to 2.4 V. Otherwise the photodiode is reset to V_{RST}.

The following reset transistor drain voltages V_{RST} have been used: 3.3 V, 2.4 V, 2.0 V and 1.6 V with sampling time set to 1.12 s. The minimum reset transistor drain voltage used is 1.6 V in order to stay in the linear part of the readout chain transfer function. The mean cathode voltage variation during integration was kept small ($\approx$ 20 mV) in comparison to the voltage step used.

The maximum electric field $E_{\max}$ in an ideal one-sided abrupt P-N$^+$ junction can be expressed as a function of the applied voltage V_{app} [19]

$$E_{\max} = \sqrt{\frac{2qN_A}{\epsilon_{\mathrm{Si}}}(V_{\mathrm{app}} + V_{\mathrm{bi}})} \tag{14}$$

with N_A the epitaxial layer uniform acceptor concentration, ϵ_{Si} the permittivity in silicon and V_{bi} the built-in voltage. By taking realistic values for CMOS image sensor photodiodes ($N_A = 10^{15}$ cm^{-3} and $V_{\mathrm{bi}} = 0.6$ V), this maximum electric field ranges from 3×10^{-4} to 2.6×10^{-4} V/cm for the photodiode cathode voltage range used. In other words, by sweeping the drain voltage from 2.4 to 1.6 V the theoretical maximum electric field is reduced by about 15%. The relationship between the maximum electric field and the local electric field in the P region at a distance x from the ideal junction is given by [19]

$$|E(x)| = \left| E_{\max} - \frac{qN_A}{\epsilon_{\mathrm{Si}}}x \right|. \tag{15}$$

This last equation shows that the local electric field decreases relatively faster than $E_{\max}$ with the applied voltage because of the last term of (15). It can then be inferred that the local electric field is reduced by more than 15% (and up to 100%) in the whole photodiode depleted region when the applied voltage drops from 2.4 to 1.6 V.

The experiment result is illustrated in Fig. 10. This figure shows the dark current evolution with time of a representative four-level RTS pixel for the four selected biasing conditions. As expected [20], we can see that the background noise almost double from soft to hard reset mode. However, the other RTS characteristics (amplitudes and time constants) remain unchanged. This is not surprising since the photodiode voltage after a soft reset is close to 2.4 V. When the reset voltage, which is equal to the cathode voltage in hard reset, decreases from 2.4 V to 1.6 V the mean dark current also decreases. This is obviously caused by the depletion region reduction which is known to decrease PN junction generation current. The left-shift observed on the mean dark current distribution (Fig. 11) shows that every pixel undergoes the same effect when the bias voltage decreases.

As regards the RTS amplitude, it is quite surprising to notice that it is not affected by the applied voltage. Indeed, the most suggested cause of the RTS large amplitudes is electric field enhancement [1], [4], [6]. Since applied electric field is assumed to be reduced by more than 15%, and since electric field enhancement is an exponential process [21], RTS amplitudes should importantly be reduced by a voltage decrease if they were greatly amplified by the electric field enhancement. The same trends can be observed on every RTS pixel. Fig. 12 presents the maximum RTS amplitude distributions. As expected from the previous conclusion, no significant change can be seen on the distributions for amplitude greater than 0.1 fA where $P(A_{\mathrm{rts}} \geq D_{\mathrm{sv}}) \approx 1$. Nevertheless, a lot more of weak transitions (< 0.1 fA) are

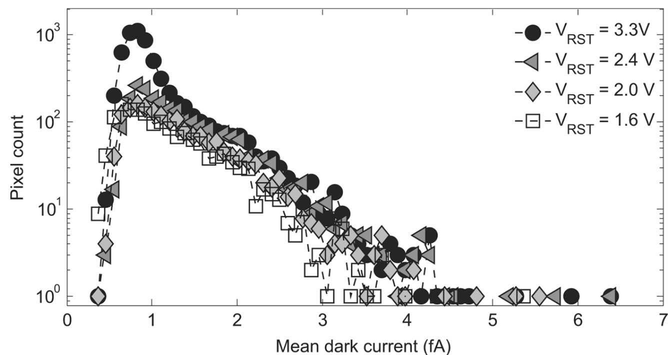

Fig. 11. Evolution of RTS pixel mean dark current distribution with reset voltage.

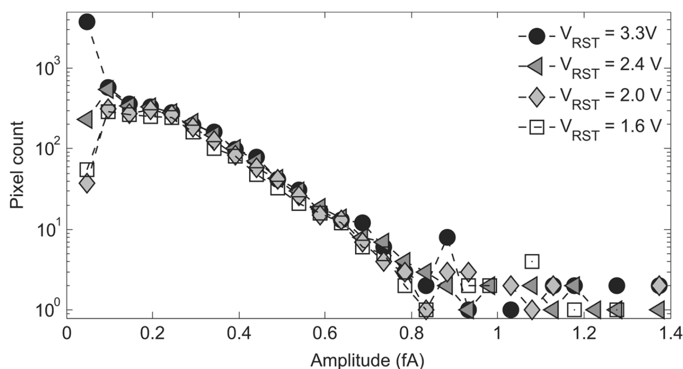

Fig. 12. Evolution of RTS amplitude distribution with reset voltage.

detected in the soft reset mode because the background noise is reduced and $P(A_{\rm rts} \geq D_{\rm sv})$ increased.

Electric field enhancement is not significant (less than a factor of ten) for electric fields lower than 7×10^4 V/cm at 23 °C [21]. This could be the reason why no sign of electric field enhancement is observed in these photodiodes where the maximum electric field is roughly assumed to be close to 3.0×10^{-4} V/cm. However, as mentioned previously, the RTS amplitudes observed are too large to be explained by the SRH generation/recombination theory. Moreover, even if field enhancement is not likely in these devices, the measured amplitudes correspond well to the amplitudes observed in previous work [1]–[9]. Hence, these observations strongly suggest that electric field enhancement is not the main cause of large RTS amplitudes. This supports the findings of Bogaerts *et al.*[4] who mention intercenter charge transfer [22] as a possible explanation for high RTS amplitudes. Nevertheless, as discussed in [9], a defect which can induce charge exchange reaction and that exhibits a switching behavior still has to be identified. Enhancement due to defect local electric field could be an alternative explanation but such an electric field is also supposed to be a function of reverse bias [23]. RTS centers are likely to be defect clusters since intercenter charge transfers, high local electric fields and generation enhancements due to local bandgap narrowing are expected in such defects [24]. Moreover, Palko and Srour have recently pointed out that amorphous inclusions exhibit similar annealing behaviors to RTS centers.

It can be noticed that the signal presented in Fig. 10 is a good example of a multilevel RTS generated by two independent RTS centers: one with a 1 fA amplitude and the other with a 0.2 fA amplitude. The disappearance of the small fluctuation on the $V_{\rm RST} = 1.6$ V plot suggests that the small amplitude RTS center is not in the depletion region for $V_{\rm RST} = 1.6$ V while the large RTS center is still located inside this volume.

IV. Summary and Conclusion

A new detection method able to automatically extract multilevel RTS parameters has been proposed. This method appears to be an efficient tool for studying a large number of RTS pixels. The first results achieved with this technique indicate that RTS maximum amplitude distributions can be divided in two parts. A peak shaped part at low amplitude, which will be studied in future work and an exponential tail for larger amplitudes. The exponential fit of this tail gave a mean maximum RTS amplitude of about 0.19 fA per RTS center at 23 °C. This value appeared to be independent of displacement damage dose. A number of defects has also been extracted and appears to increase linearly with displacement damage dose with the following factor: 47 centers $\cdot$ cm^{-3} $\cdot$ (MeV/g)$^{-1}$. Thanks to these two parameters, RTS amplitude distributions can be predicted. The fluences used in this study seem too high to produce optimum RTS level distributions and lower fluences will be used in future studies. The effect of applied electric field, through the variation of photodiode reset voltage, has also been studied. As expected, the decrease of bias voltage reduced the mean dark current generation through a depletion region reduction. However, no change in RTS amplitude was observed. This suggests that electric field enhancement due to the applied bias does not play an important role in the RTS center generation enhancement. Intercenter charge transfer and defect cluster related effects seem to be promising explanations for these high amplitudes.

As already mentioned, future work should focus on larger arrays and lower fluences to confirm these first results. The next step will be the use of the transition time constant extraction feature provided by the new method for studying more in detail the origin of multilevel RTS.

Acknowledgment

The authors would like to thank L. Duvet from ESA, F. Bezerra and S. Petit from CNES, and T. Nuns from ONERA for proton irradiation opportunities. They would also like to thank P. Cervantes, P. Pinel, C. Engel, F. Corbière, and N. Huger from ISAE for their help with software development, circuit design, packaging, and experimental issues, as well as L. Boucher and I. Djite for their stimulating discussions.

References

[1] I. H. Hopkins and G. R. Hopkinson, "Random telegraph signals from proton-irradiated CCDs," *IEEE Trans. Nucl. Sci.*, vol. 40, no. 6, pp. 1567–1574, Dec. 1993.

[2] I. H. Hopkins and G. R. Hopkinson, "Further measurements of random telegraph signals in proton-irradiated CCDs," *IEEE Trans. Nucl. Sci.*, vol. 42, no. 6, pp. 2074–2081, Dec. 1995.

[3] G. R. Hopkinson, "Radiation effects in a CMOS active pixel sensor," *IEEE Trans. Nucl. Sci.*, vol. 47, no. 6, pp. 2480–2484, Dec. 2000.
[4] J. Bogaerts, B. Dierickx, and R. Mertens, "Random telegraph signal in a radiation-hardened CMOS active pixel sensor," *IEEE Trans. Nucl. Sci.*, vol. 49, no. 1, pp. 249–257, Feb. 2002.
[5] A. M. Chugg, R. Jones, M. J. Moutrie, J. R. Armstrong, D. B. S. King, and N. Moreau, "Single particle dark current spikes induced in CCDs by high energy neutrons," *IEEE Trans. Nucl. Sci.*, vol. 50, no. 6, pp. 2011–2017, Dec. 2003.
[6] D. R. Smith, A. D. Holland, and I. B. Hutchinson, "Random telegraph signals in charge coupled devices," *Nucl. Instrum. Meth. A*, vol. 530, no. 3, pp. 521–535, Sep. 2004.
[7] T. Nuns, G. Quadri, J.-P. David, O. Gilard, and N. Boudou, "Measurements of random telegraph signal in CCDs irradiated with protons and neutrons," *IEEE Trans. Nucl. Sci.*, vol. 53, no. 4, pp. 1764–1771, Aug. 2006.
[8] T. Nuns, G. Quadri, J.-P. David, and O. Gilard, "Annealing of proton-induced random telegraph signal in CCDs," *IEEE Trans. Nucl. Sci.*, vol. 54, no. 4, pp. 1120–1128, Aug. 2007.
[9] G. R. Hopkinson, V. Goiffon, and A. Mohammadzadeh, "Random telegraph signals in proton irradiated CCDs and APS," *IEEE Trans. Nucl. Sci.*, vol. 55, no. 4, pp. 2197–2204, Aug. 2008.
[10] Y. Yuzhelevski, M. Yuzhelevski, and G. Jung, "Random telegraph noise analysis in time domain," *Rev. Sci. Instrum.*, vol. 71, no. 4, pp. 1681–1688, Apr. 2000.
[11] A. Konczakowska, J. Cichosz, and A. Szewczyk, "A new method for RTS noise of semiconductor devices identification," *IEEE Trans. Instrum. Meas.*, vol. 57, no. 6, pp. 1199–1206, Jun. 2008.
[12] C. J. Dale, L. Chen, P. J. M. Nulty, P. W. Marshall, and E. A. Burke, "A comparison of monte carlo and analytical treatments of displacement damage in Si microvolumes," *IEEE Trans. Nucl. Sci.*, vol. 41, no. 6, pp. 1974–1983, Dec. 1994.
[13] P. Marshall, C. Dale, and E. Burke, "Proton-induced displacement damage distributions and extremes in silicon microvolumes charge injection device," *IEEE Trans. Nucl. Sci.*, vol. 37, no. 6, pp. 1776–1783, Dec. 1990.
[14] M. Robbins, "High-energy proton-induced dark signal in silicon charge coupled devices.," *IEEE Trans. Nucl. Sci.*, vol. 47, no. 6, pp. 2473–2479, Dec. 2000.
[15] P. Marshall, C. Dale, E. Burke, G. Summers, and G. Bender, "Displacement damage extremes in silicon depletion regions," *IEEE Trans. Nucl. Sci.*, vol. 36, no. 6, pp. 1831–1839, Dec. 1989.
[16] W. Shockley and W. T. Read, "Statistics of the recombinations of holes and electrons," *Phys. Rev.*, vol. 87, no. 5, pp. 835–842, Sep. 1952.
[17] D. K. Schroder, *Semiconductor Material and Device Characterization*, 2nd ed. New York: Wiley Interscience, 1998.
[18] B. Pain, G. Yang, T. J. Cunningham, C. Wrigley, and B. Hancock, "An enhanced-performance CMOS imager with a flushed-reset photodiode pixel," *IEEE Trans. Electron Devices*, vol. 50, no. 1, pp. 48–56, Jan. 2003.
[19] S. M. Sze, *Physics of Semiconductor Devices*, 2nd ed. New York: Wiley, 1981.
[20] H. Tian, B. Fowler, and A. El Gamal, "Analysis of temporal noise in CMOS photodiode active pixel sensor," *IEEE J. Solid-State Circuits*, vol. 36, no. 1, pp. 92–101, Jan. 2001.
[21] G. Vincent, A. Chantre, and D. Bois, "Electric field effect on the thermal emission of traps in semiconductor junctions," *J. Appl. Phys.*, vol. 50, no. 8, pp. 5484–5487, 1979.
[22] S. Watts, J. Matheson, I. Hopkins-Bond, A. Holmes-Siedle, A. Mohammadzadeh, and R. Pace, "A new model for generation-recombination in silicon depletion regions after neutron irradiation," *IEEE Trans. Nucl. Sci.*, vol. 43, no. 6, pp. 2587–2594, Dec. 1996.
[23] A. Czerwinski, "Defect-related local-electric-field impact on p–n junction parameters," *Appl. Phys. Lett.*, vol. 75, no. 25, pp. 3971–3973, 1999.
[24] J. W. Palko and J. R. Srour, "Amorphous inclusions in irradiated silicon and their effects on material and device properties," *IEEE Trans. Nucl. Sci*, vol. 55, no. 6, pp. 2992–2999, Dec. 2008.